



Insight into crystal growth and upconversion luminescence property of tetragonal $\text{Ba}_3\text{Sc}_2\text{F}_{12}$ nanocrystals

Juan Xie, Guang-Chao Zheng, Yang-Ming Hu, Farhat Nosheen, Zhi-Cheng Zhang* ,
Er-Jun Liang* 

Received: 13 August 2020/Revised: 18 September 2020/Accepted: 5 October 2020/Published online: 25 November 2020
© GRINM Bohan (Beijing) Publishing Co., Ltd 2020

Abstract Sc-based nanomaterials have attracted considerable attention due to their unique optical properties different from those of Ln/Y-based nanomaterials. However, studies on Sc-based nanomaterials are far from comprehensive. Particularly, nanoscale alkaline (Ca, Sr and Ba) scandium fluorides were almost ignored for their stringent synthetic conditions. Herein, we synthesize high-quality tetragonal phase $\text{Ba}_3\text{Sc}_2\text{F}_{12}$ nanocrystals with uniform morphology and good dispersibility by carefully tailoring the reaction conditions, such as the molar ratio of reactants, temperature and reaction time. Then, the upconversion (UC) luminescence property of $\text{Ba}_3\text{Sc}_2\text{F}_{12}:\text{Yb}/\text{Er}$ (Ho) samples is investigated in detail. The doping concentrations of sensitizer (Yb^{3+}) and activator (Er^{3+} and Ho^{3+}) are optimized for the strongest UC luminescence, of which the corresponding energy transfer processes are also discussed. Moreover, tetragonal $\text{Ba}_3\text{Sc}_2\text{F}_{12}$ nanocrystals can gradually transform into hexagonal $\text{Ba}_4\text{Yb}_3\text{F}_{17}$ nanocrystals with the

increase in Yb^{3+} doping content. This work provides a novel type of Sc-based nanomaterials with strong red UC emissions which are promising in high-resolution 3-dimensional color displays, laser, bioimaging and biolabels.

Keywords $\text{Ba}_3\text{Sc}_2\text{F}_{12}$ nanocrystals; Crystal growth; Upconversion; Sc-based nanomaterials

1 Introduction

Lanthanide-doped upconversion nanoparticles (UCNPs) have attracted considerable attentions as a result of their outstanding luminescent performance compared with traditional photoluminescent (PL) nanomaterials such as fluorescent organic dyes and quantum dots (QDs) [1–7]. Owing to their fine photostability, low photobleaching, long lifetimes, minimal phototoxicity and deep penetration depth [8–10], UCNPs are promising in three-dimensional (3D) flat panel displays [11], white light emitting diodes [12, 13], solar cells [14], and especially in biolabels and bioimaging [15–18]. However, UCNPs remain suffering from weak luminescent intensity, low efficiency, high power excitation and a confined excitation wavelength during UC process [19–23]. During last decades, a lot of efforts have been made to enhance UC intensity, such as broadband sensitization [24, 25], surface passivation [26–29], energy transfer modulation [30, 31], surface plasmon coupling [32]. In addition, exploring new host matrix is also an efficient method, because the local crystal field of host matrix and the interaction between host and doping ions have a strong impact on the UC process. As widely confirmed, host lattice determines the distance, spatial position, coordination numbers and the type of surrounding anions of doping ions [33, 34].

Electronic supplementary material The online version of this article (<https://doi.org/10.1007/s12598-020-01631-x>) contains supplementary material, which is available to authorized users.

J. Xie, G.-C. Zheng, Y.-M. Hu, E.-J. Liang*
School of Physics and Microelectronics, Zhengzhou University,
Zhengzhou 450001, China
e-mail: ejliang@zzu.edu.cn

F. Nosheen
Division of Science and Technology, Department of Chemistry,
University of Education, Lahore 54770, Pakistan

Z.-C. Zhang*
Tianjin Key Laboratory of Molecular Optoelectronic Sciences,
Department of Chemistry, School of Science, Tianjin University
and Collaborative Innovation Center of Chemical Science and
Engineering, Tianjin 300072, China
e-mail: zczhang19@tju.edu.cn

As a recently prevalent topic, Sc-based nanomaterials have become hotspots. Sc belongs to the rare earth family. However, it has no 4f electrons and behaves more like transition metals, which endows Sc-based nanomaterials unique properties, such as different UC luminescence behaviors from those of Y/Ln-based nanomaterials and remarkable negative thermal expansion constant [35–39]. Currently, alkali (Na, K, Rb, Cs) scandium fluorides with various morphologies and size including M_2NaScF_6 ($M = K, Rb, Cs$), $NaScF_4$, Na_3ScF_6 and KSc_2F_7 have been synthesized and investigated [40–44]. However, alkaline earth ions (Ca^{2+} , Sr^{2+} and Ba^{2+}) owning closed ionic radii with lanthanide ions were almost ignored. Recently, Yang's group have successfully synthesized $SrSc_2F_7$ and $Ba_3Sc_2F_{12}$ crystals with various morphologies by hydrothermal process and investigated the fluorescence of the new host, which indicates that $SrSc_2F_7$ and $Ba_3Sc_2F_{12}$ are excellent host material for UC luminescence [45, 46]. However, the research on synthesis and UC luminescence properties of nanoscaled alkaline rare earth fluorides with uniform morphology, and good dispersibility is still absent to the best of our knowledge.

Herein, we report the precise synthesis of $Ba_3Sc_2F_{12}$ nanocrystals by thermolysis method. The synthesis conditions, including temperature, reaction time and ratio of reactants, are optimized to control the crystal growth process and to get high-quality products. Then, we carefully explore the UC luminescence properties of Yb/Er and Yb/Ho doped $Ba_3Sc_2F_{12}$ nanocrystals and the corresponding energy transfer mechanisms. In order to obtain the strongest UC luminescent intensity, we modify the doping concentration of sensitizer ions Yb^{3+} from 10 mol% to 98 mol% and activator ions Er^{3+} or Ho^{3+} from 1 mol% to 8 mol%. We also notice that with Yb^{3+} doping concentration increasing, pure tetragonal phase $Ba_3Sc_2F_{12}$ can gradually transform to hexagonal phase $Ba_4Yb_3F_{17}$ nanocrystals.

2 Experimental

2.1 Materials

Sc_2O_3 (99.99%), Yb_2O_3 (99.99%), Er_2O_3 (99.99%), Ho_2O_3 (99.99%) and $Ba(CH_3COO)_2$ (99.99%) were purchased from HWRK Chem Co. Ltd. (Beijing China). CF_3COOH (99%) was obtained from Lingfeng Chemical Reagent Co. Ltd. (Shanghai China). Oleic acid (OA, 90%) and 1-octadecene (ODE, 90%) were purchased from Sigma-Aldrich. All the materials were used directly without further purification.

2.2 Characterization

Powder X-ray diffraction (XRD) data were recorded via a Rigaku D/max 2550 with $Cu K\alpha$ radiation ($\lambda = 0.15418$ nm). The morphology and size of nanocrystals were analyzed by the Hitachi 7700 transmission electron microscope (TEM) with an acceleration voltage of 100 kV. High-resolution TEM (HRTEM) images were obtained through Tecnai G2 F20 field emission transmission electron microscope (FESEM) equipped with an energy-dispersed X-ray system (EDX) operating at 200 kV. Inductively coupled optical emission spectrometry (ICP-OES) analysis was performed on a PE Optima 5300DV spectrometer. The UC luminescence spectra were collected using an Edinburgh F920 spectrometer with an external continuous wave diode 980 nm laser at room temperature. All luminescence studies were carried out under identical conditions.

2.3 Synthesis of $RE(CF_3COO)_3$ precursors ($RE = Sc, Yb, Er, Ho$)

In a typical synthesis, RE_2O_3 (2 mmol) was dissolved in 2 ml deionized water under vigorous magnetic stirring. CF_3COOH was added to above mixture at room temperature. Then, the solution was heated to 100 °C and kept for 12 h until the solution became transparent. The final products were dried in a vacuum oven at 60 °C for 24 h.

2.4 Synthesis of $Ba_3Sc_2F_{12}:Yb/Er$ nanocrystals

In a typical synthesis, 0.200 mmol $Ba(CH_3COO)_2$, 0.312 mmol $Sc(CF_3COO)_3$, 0.080 mmol $Yb(CF_3COO)_3$ and 0.008 mmol $Er(CF_3COO)_3$ were added into a 100 ml three-necked round-bottom flask containing 17 ml oleic acid and 3 ml octadecene. The mixture was heated to 120 °C and kept for 30 min with magnetic stirring under an argon atmosphere. Subsequently, the mixture was heated to 310 °C and maintained for 50 min before cooling down to room temperature. Finally, the as-prepared samples were precipitated by addition of ethanol, collected by centrifugation at 9000 $r \cdot min^{-1}$ for 5 min, washed with water and ethanol several times, and finally redispersed in cyclohexane for further characterization.

3 Results and discussion

$Ba_3Sc_2F_{12}$ and lanthanide ions doped $Ba_3Sc_2F_{12}$ nanocrystals were prepared via the modified thermolysis method [47]. The crystal growth process is clearly presented in Fig. 1, where oleic acid (OA) was used as surfactant and noncoordinating 1-octadecene (ODE) as

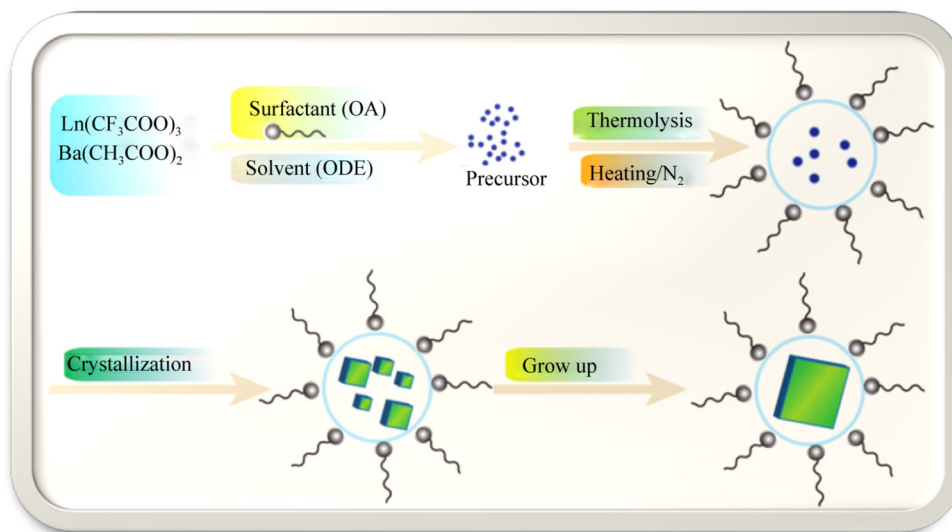


Fig. 1 Scheme of growth process of Ba₃Sc₂F₁₂ and Ba₃Sc₂F₁₂:Ln (Ln = Yb, Er, Ho) nanocrystals via thermolysis method

reaction solvent for its high boiling point. The carboxyl group of OA can coordinate the rare earth elements, while the long hydrocarbon chain acts as a passivating ligand which can prevent the final nanoparticles from agglomeration. Then, by carefully tailoring experimental conditions, high-quality Ba₃Sc₂F₁₂ nanocrystals with great dispersibility, narrow size distribution and good crystallinity could be readily acquired.

Figure 2a1–e1 shows the effect of Ba²⁺ content on the morphology and crystal structure of Ba₃Sc₂F₁₂:Yb/Er nanocrystals. At low Ba²⁺ content, most of the products were irregular nanoparticles and only few tetragonal nanosheets were observed (Fig. 2a1). XRD data indicate that the products are mixture of cubic phase ScF₃ and tetragonal phase Ba₃Sc₂F₁₂ (Fig. 2e1). With the increase in Ba²⁺ content, pure tetragonal phase Ba₃Sc₂F₁₂ could be acquired. When the molar ratio of Ba²⁺ to Sc³⁺ was 0.50, uniform and well dispersed Ba₃Sc₂F₁₂ nanosheets were synthesized and the particle size was about 35 nm × 35 nm. However, at high Ba²⁺ content (Ba:Sc = 2.00), majority of products were tetragonal nanosheets with the size of 5 nm × 5 nm. These results indicate that Ba²⁺ content has considerable influence on the shape and phase evolution of Ba₃Sc₂F₁₂ nanocrystals and that appropriate Ba²⁺ content is crucial to the synthesis of uniform and pure Ba₃Sc₂F₁₂ nanocrystals.

The morphology and phase development caused by Ba²⁺ content can be explained by the crystallization speed-controlled model [48–50]. The nanocrystal growth was initiated with the nucleation process of Ba²⁺, Sc³⁺ and F⁻. In addition, the change of monomer concentration in the solution is mainly caused by the nucleation process, while the following growth process has relatively slight impact.

The precursors in our experiments were Ba(CH₃COO)₂ and Sc(CF₃COO)₃, while the ratio of F⁻ to Sc³⁺ was set as 3, so the ratios of F⁻ to Ba²⁺ and Ba²⁺ to Sc³⁺ changed depending on the amount of Ba²⁺ added. Low concentration of Ba²⁺ shall decelerate the particle crystallization rate and produce relatively small number of nuclei, leading to a high monomer concentration, so highly uniform tetragonal Ba₃Sc₂F₁₂ nanosheets were obtained under Ba²⁺:Sc³⁺ = 0.50. However, according to the mechanism of chemical reaction equilibrium, Ba²⁺ content was too low to form Ba₃Sc₂F₁₂ when the ratio of Ba²⁺ to Sc³⁺ was 0.25, so the cubic phase ScF₃ was obtained. On the contrary, high Ba²⁺ content can enhance the crystallization speed which results in rapid depletion of RE(CF₃COO)₃ in the solution. When the monomer concentration was reduced to a critical level rapidly, Ba₃Sc₂F₁₂ nanocrystals with smaller size and worse crystallinity appeared.

Then, the effect of the reaction temperature on the morphology and crystal structure of Ba₃Sc₂F₁₂ nanocrystals were explored. Corresponding results are listed in Fig. 2a2–e2. At 280 and 290 °C, most of the products were of irregular morphology and only little tetragonal Ba₃Sc₂F₁₂ nanosheets were obtained. XRD results in Fig. 2e2 show that the products were not pure tetragonal phase. As the reaction temperature increased to 300 °C, pure tetragonal phase was acquired. However, the morphology was not uniform and many small round Ba₃Sc₂F₁₂ nanosheets were still obtained. XRD results show that the products were only pure tetragonal phase. Further increase the temperature to 310 °C, uniform tetragonal nanosheets with an average size of 35 nm × 35 nm were acquired. Herein, 310 °C was suitable temperature to synthesize uniform Ba₃Sc₂F₁₂ nanocrystals.

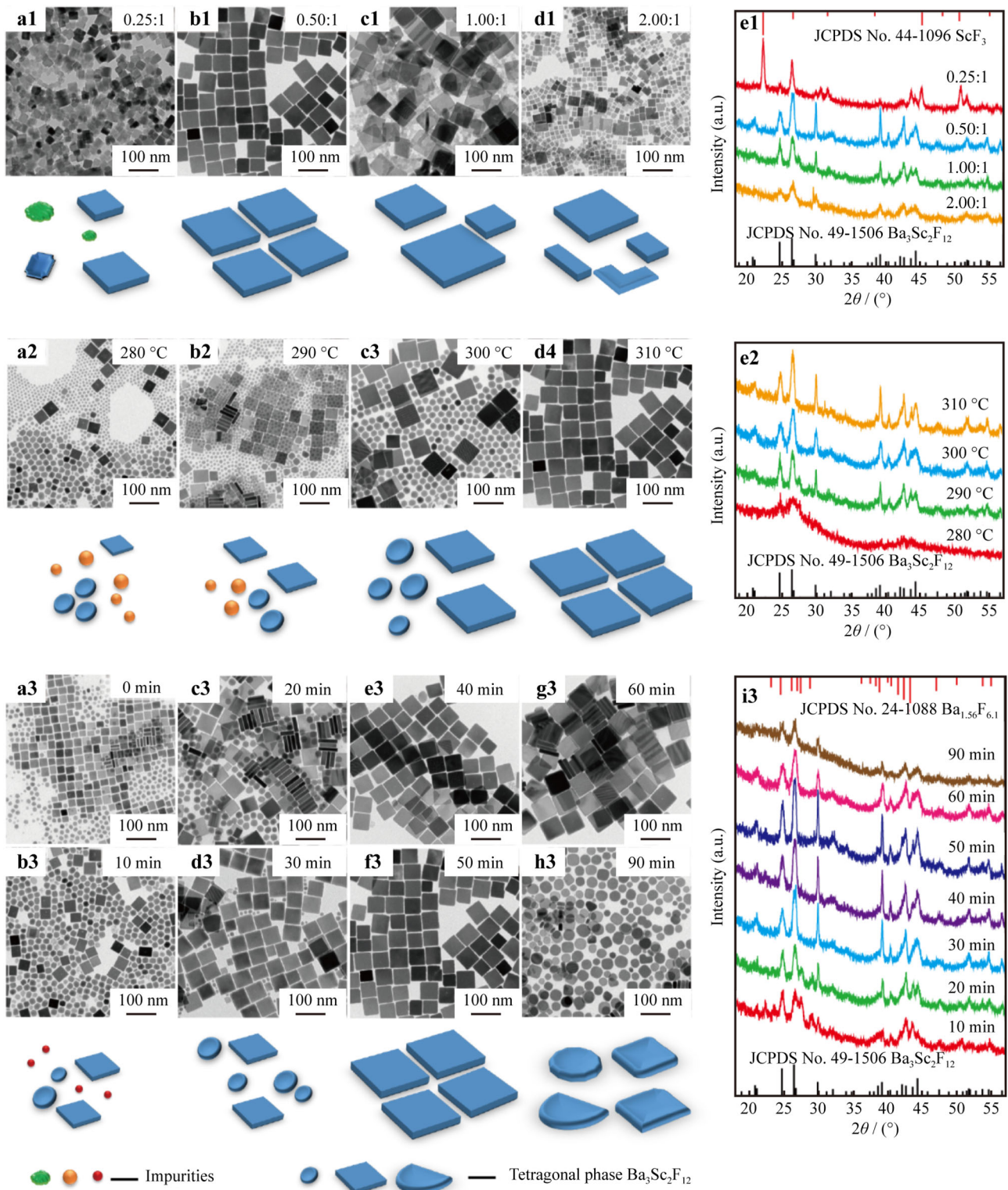


Fig. 2 $\text{Ba}_3\text{Sc}_2\text{F}_{12}$ nanocrystals synthesized under different reaction conditions: **a1–d1** TEM images and **e1** XRD patterns of $\text{Ba}_3\text{Sc}_2\text{F}_{12}$ nanocrystals synthesized under different ratios of Ba to Sc (0.25, 0.50, 1.00, 2.00); **a2–d2** TEM images and **e2** XRD patterns of $\text{Ba}_3\text{Sc}_2\text{F}_{12}$ nanocrystals synthesized at 280, 290, 300 and 310 °C, respectively; **a3–h3** TEM images and **i3** XRD patterns of $\text{Ba}_3\text{Sc}_2\text{F}_{12}$ nanocrystals synthesized at different reaction time (0, 10, 20, 30, 40, 50, 60, 90 min)

In order to track the morphology and phase evolution of $\text{Ba}_3\text{Sc}_2\text{F}_{12}$ nanocrystals, we monitored the nanocrystal growth process. As is shown in Fig. 2a3–h3, when the reaction time was set as 0, 10 or 20 min, the products were composed of irregular small nanoplates and little small tetragonal nanosheets. Corresponding XRD results indicate the existence of impurities (Fig. 2i3). When the reaction was prolonged to 30 min, pure tetragonal phase $\text{Ba}_3\text{Sc}_2\text{F}_{12}$ nanocrystals could be obtained, which can be seen from the XRD patterns. TEM images show fewer small irregular and more uniform tetragonal nanosheets as the time increased. However, when the reaction time was prolonged to 90 min, the corners and tips of tetragonal nanosheets were smoothed and TEM images show irregular nanoparticles. TEM images of $\text{Ba}_3\text{Sc}_2\text{F}_{12}$ nanocrystals at different reaction time in Fig. 2a3–h3 obviously demonstrate a typical Ostwald ripening process [51, 52]. In addition, 50 min was enough for $\text{Ba}_3\text{Sc}_2\text{F}_{12}$ nanocrystals ripening process.

Based on the above results and discussion, we knew that the suitable ratio of Ba^{2+} to Sc^{3+} was 0.5, the best reaction temperature was 310 °C and 50 min was enough for the synthesis of $\text{Ba}_3\text{Sc}_2\text{F}_{12}$ nanocrystals in current system.

To explore the UC luminescence property and to get the strongest UC luminescence intensity of $\text{Ba}_3\text{Sc}_2\text{F}_{12}$ nanocrystals, we synthesized a series of $\text{Ba}_3\text{Sc}_2\text{F}_{12}:\text{Yb}/\text{Er}$ ($x/2$ mol%) nanocrystals under above optimized conditions of which the ratio of Ba^{2+} to Sc^{3+} is 0.50, reaction temperature is 310 °C and reaction time is 50 min. The doping content of sensitizer ion Yb^{3+} was tuned from 10 mol% to 98 mol% firstly. Corresponding TEM images and XRD patterns are listed in Fig. 3. When the concentrations of Yb^{3+} were 10 mol%–30 mol%, the products obtained were pure tetragonal phase $\text{Ba}_3\text{Sc}_2\text{F}_{12}$ nanocrystals with uniform size. With the concentration of Yb^{3+} further increasing to 40 mol%–50 mol%, the products became big tetragonal nanosheets mixed with irregular small nanosheets, which were tetragonal phase $\text{Ba}_3\text{Sc}_2\text{F}_{12}$ and tetragonal phase $\text{Ba}_4\text{Yb}_3\text{F}_{17}$, respectively. When the concentration of Yb^{3+} was more than 60 mol%, the products were pure tetragonal phase $\text{Ba}_4\text{Yb}_3\text{F}_{17}$. Inductively coupled plasma mass spectroscopy (ICP-MS) analysis was carried out to characterize the actual concentration of Yb^{3+} doped into the as-synthesized $\text{Ba}_m\text{Sc}_{1-x}\text{F}_n:\text{Yb}/\text{Er}$ ($x/2$ mol%) nanocrystals, which are listed in Table S1. Considering the same charge and adjacent ionic radii of Sc^{3+} (0.0745 nm) and Yb^{3+} (0.0868 nm), we believe that Yb^{3+} has substituted Sc^{3+} . Figure S1 shows the evolution of (310) diffraction patterns of $\text{Ba}_3\text{Sc}_2\text{F}_{12}:\text{Yb}/\text{Er}$ ($x/2$ mol%). As Yb^{3+} substitutes Sc^{3+} , the unit cell of $\text{Ba}_3\text{Sc}_2\text{F}_{12}$ would swell, leading to the shift of XRD peak to small angles according to the Bragg's law, which is consistent with XRD results.

To prove the transformation process from pure tetragonal phase $\text{Ba}_3\text{Sc}_2\text{F}_{12}$ to hexagonal $\text{Ba}_4\text{Yb}_3\text{F}_{17}$, TEM and

high-resolution TEM (HRTEM) images of 20 mol%, 40 mol% and 80 mol% Yb^{3+} doped samples are presented in Fig. S2. The HRTEM image of 20 mol% doped sample reveals a highly crystalline nature and the interplanar distance between the adjacent lattice fringes is 0.299 nm, which matches well with (310) lattice planes of tetragonal phase $\text{Ba}_3\text{Sc}_2\text{F}_{12}$. The HRTEM image of 80 mol% Yb^{3+} doped product shows that the interplanar distance between the adjacent lattice fringes is 0.294 nm, which agrees well with (214) lattice planes of hexagonal phase $\text{Ba}_4\text{Yb}_3\text{F}_{17}$. While 40 mol% Yb^{3+} doped products are the mixture of tetragonal phase $\text{Ba}_3\text{Sc}_2\text{F}_{12}$ and hexagonal $\text{Ba}_4\text{Yb}_3\text{F}_{17}$ nanocrystals. The two crystal structures grow independently and exist as a physical mixture rather than, for example, as core–shell particles [39].

Similar results were also observed when 2 mol% Ho^{3+} ions were used as activator. Corresponding TEM images and XRD patterns are listed in Fig. S3, which indicate that $\text{Ba}_m\text{Sc}_{1-x}\text{F}_n:\text{Yb}/\text{Ho}$ ($x/2$ mol%) nanocrystals transform from pure tetragonal $\text{Ba}_3\text{Sc}_2\text{F}_{12}:\text{Yb}/\text{Ho}$ to $\text{Ba}_4\text{Yb}_3\text{F}_{17}:\text{Sc}/\text{Ho}$ with Yb^{3+} concentration varying from 0 mol% to 98 mol%.

Figure 4a displays UCPL emission spectra of $\text{Ba}_m\text{Sc}_{1-x}\text{F}_n:\text{Yb}/\text{Er}$ ($x/2$ mol%) nanocrystals with variable Yb^{3+} concentration from 0 mol% to 98 mol%. All samples exhibit strong red UC luminescence, which is contrary to $\text{NaYF}_4:\text{Yb}/\text{Er}$ (20/2 mol%) nanocrystals that generate strong green UC emission under 980-nm laser excitation. The UC emission intensity of the products also changed with the variation of Yb^{3+} concentration. When Yb^{3+} concentration varied from 0 mol% to 25 mol%, the UC luminescence intensity of $\text{Ba}_3\text{Sc}_2\text{F}_{12}:\text{Yb}/\text{Er}$ nanocrystals increased gradually. As is known to us all, Yb^{3+} has a sufficient absorption cross section matching well with common 980-nm laser excitation source. Herein, we reason that introduction of an elevated amount of Yb^{3+} dopants in the $\text{Ba}_3\text{Sc}_2\text{F}_{12}$ host lattice decreases $\text{Yb}^{3+}-\text{Er}^{3+}$ interatomic distance and thus facilitates energy transfer from Yb^{3+} to Er^{3+} . In addition, high Yb^{3+} contents help sustain multi-step excitation without depletion of the intermediate, which will benefit UC luminescence process. However, as the Yb^{3+} ions content further increased from 25 mol% to 98 mol%, the luminescent intensity fell down quickly as a result of concentration quenching phenomenon, which means that a high Yb^{3+} content leads to an increased possibility of long-distance energy transfer that takes excitation energy to lattice or surface defects instead of luminescence [53, 54]. So, for $\text{Ba}_3\text{Sc}_2\text{F}_{12}:\text{Yb}/\text{Er}$ system, the optimum Yb^{3+} concentration for efficient UC under 980-nm excitation was 25 mol%.

Then, we optimized Er^{3+} concentration. ICP-MS analysis of the actual concentration of Er^{3+} doped into the as-synthesized $\text{Ba}_3\text{Sc}_2\text{F}_{12}:\text{Yb}/\text{Er}$ (25/ x mol%) nanocrystals is

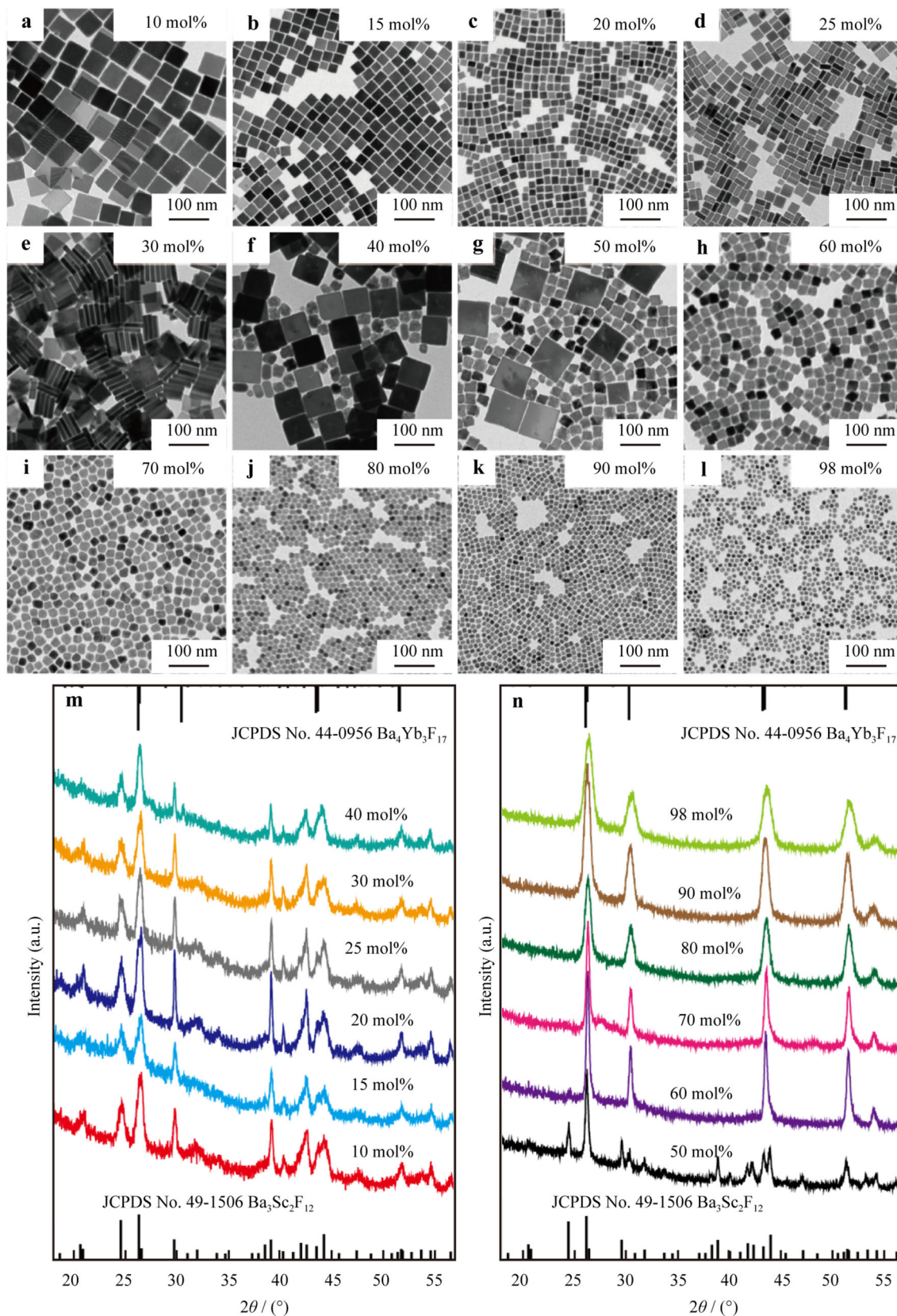


Fig. 3 a–l TEM images and m, n XRD patterns of $\text{Ba}_m\text{Sc}_{1-x}\text{Yb}_x\text{F}_n$: Er (2 mol%) with different amounts of Yb^{3+} doped ($x = 10 \text{ mol\%}–98 \text{ mol\%}$)

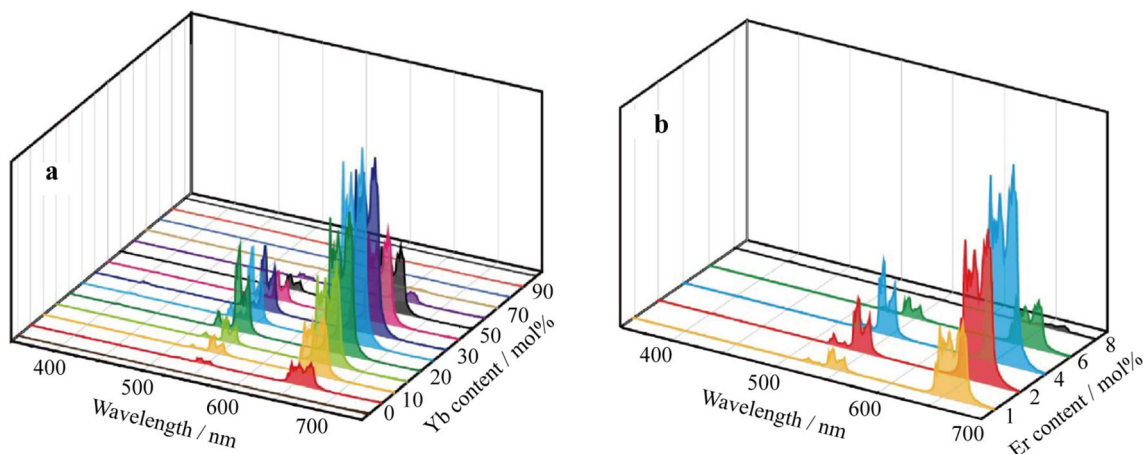


Fig. 4 **a** UC emission spectra of $\text{Ba}_m\text{Sc}_{1-x}\text{Yb}_x\text{F}_n:\text{Er}$ (2 mol%) ($x = 0, 10, 15, 20, 25, 30, 40, 50, 60, 70, 80, 90$ and 98 , mol%); **b** UC emission spectra of $\text{Ba}_3\text{Sc}_2\text{F}_{12}:\text{Yb}/\text{Er}$ (25 mol%/ x mol%) ($x = 1, 2, 4, 6$ and 8 , mol%) under the excitation of 980-nm NIR diode laser at room temperature

given in Table S2. Figure 4b shows the UC luminescence spectra of $\text{Ba}_3\text{Sc}_2\text{F}_{12}:\text{Yb}/\text{Er}$ (25/ x mol%) nanocrystals with variable Er^{3+} contents ranging from 1 mol% to 8 mol%. As an elevated amount of Er^{3+} dopants will increase the amount of UC emission centers, the UC intensity becomes stronger and stronger as the Er^{3+} contents increase from 1 mol% to 4 mol%. However, more than 4 mol% Er^{3+}

doping would lead to the decrease in intensity because high doping level could inevitably lead to localized concentration quenching of activator emissions caused by enhanced cross relaxation between the lanthanide ions. Herein, the optimal Er^{3+} content is 4 mol%.

For the case of activator Ho^{3+} , we also optimized the doping content of Yb^{3+} . The UC luminescence spectra of

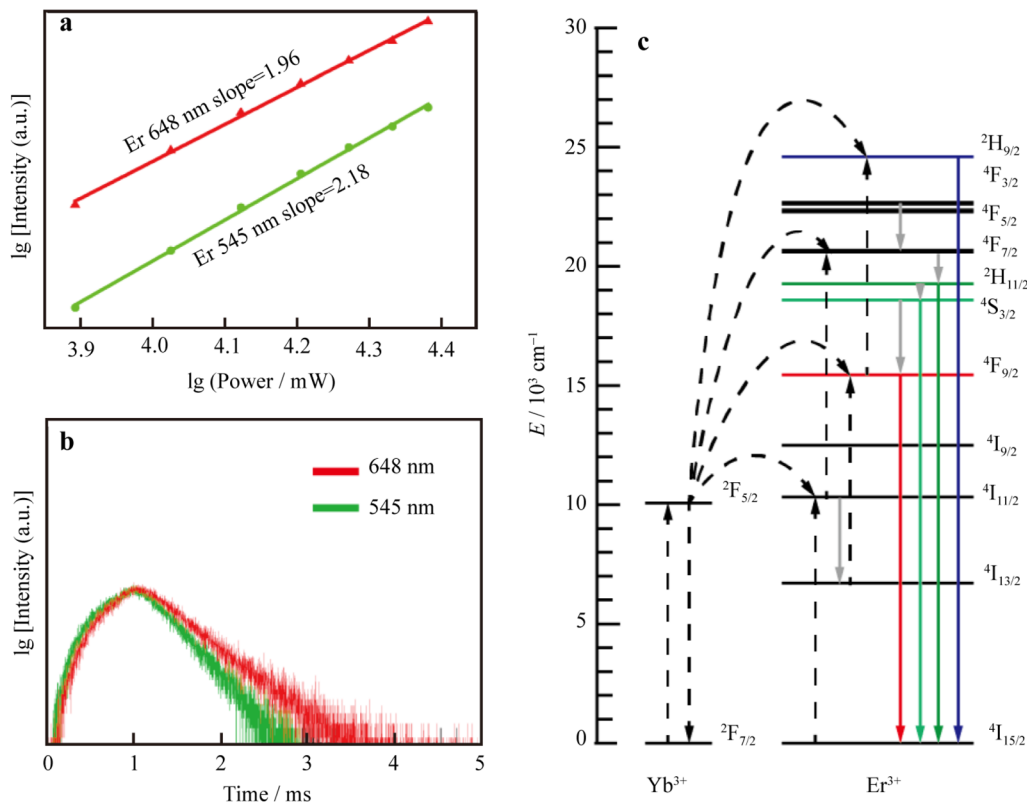


Fig. 5 **a** lg–lg plots of UC emission intensity in 648 nm (red) and 548 nm (green) intensity for $\text{Ba}_3\text{Sc}_2\text{F}_{12}:\text{Yb}/\text{Er}$ (25 mol%/4 mol%) nanocrystals; **b** luminescent decay curves of Er^{3+} in 648 nm (red) and 548 nm (green); **c** proposed UC mechanism under excitation of 980-nm NIR diode laser at room temperature (E : energy)

$\text{Ba}_3\text{Sc}_2\text{F}_{12}:\text{Yb}/\text{Ho}$ ($x/2$ mol%) nanocrystals are exhibited in Fig. S4a, which shows that the optimal Yb^{3+} content was 30 mol%. Then, we changed the concentration of Ho^{3+} from 1 mol% to 8 mol%, finding that the optimal Ho^{3+} content for $\text{Ba}_3\text{Sc}_2\text{F}_{12}:\text{Yb}/\text{Ho}$ ($30/x$ mol%) was 4 mol%, of which the results are shown in Fig. S4b. The actual concentrations of Yb^{3+} and Ho^{3+} doped into the as-synthesized $\text{Ba}_3\text{Sc}_2\text{F}_{12}:\text{Yb}/\text{Ho}$ samples are listed in Tables S3, S4, respectively.

To further understand the underlying UC mechanism of $\text{Ba}_3\text{Sc}_2\text{F}_{12}:\text{Yb}/\text{Er}$ (25/4 mol%), we explored the number of photons involved in the UC luminescence process (Fig. 5a) and UC lifetime (Fig. 5b). According the equation $I \propto P^n$, where I represents the UC luminescence intensity, P is the pumping power, and n is the number of required pumping photons; the emission intensity (I) is proportional to P^n . The logarithmic curves between the UC emission intensity and pumping power are shown in Fig. 5a, where the slope of each curve denotes the number of photons required. Based on the value of n presented in Fig. 5a, the UC emissions of 545 and 654 nm all follow a two-photon process. The decay time of energy transition from $^4\text{S}_{3/2}$ and $^4\text{F}_{9/2}$ to $^4\text{I}_{15/2}$ for Er^{3+} is 0.54 and 0.41 ms, respectively. Figure 5c shows the proposed mechanism of UC emission spectra of $\text{Ba}_3\text{Sc}_2\text{F}_{12}:\text{Yb}/\text{Er}$ (25/4 mol%) nanocrystals. Under 980-nm laser excitation, Yb^{3+} can be excited to $^4\text{F}_{5/2}$ level, from where it transfers its energy to the nearby Er^{3+} $^4\text{I}_{11/2}$ state and returns to its ground state. Populating on the metastable level $^4\text{I}_{11/2}$, Er^{3+} can be either excited to its higher state $^4\text{F}_{7/2}$ via absorbing another photon or relax to its lower state $^4\text{I}_{13/2}$ via non-radiative transition from the level $^4\text{I}_{13/2}$. Er^{3+} can also be excited to its higher state $^4\text{F}_{9/2}$ by absorbing a 980-nm photon. The transition of Er^{3+} at $^4\text{F}_{9/2}$ state to the ground state gives rise to a 654-nm photon, while the Er^{3+} at $^4\text{F}_{7/2}$ state will relax to $^2\text{H}_{11/2}$ and $^4\text{S}_{3/2}$, from where they emit 525, 545 nm photons and transit back to the ground state $^4\text{I}_{15/2}$. For Ho^{3+} , the red (654 nm) and green (545 nm) emission originates from the characteristic radiative transition from $^5\text{F}_5$ and $^5\text{F}_4$ of Ho^{3+} to its $^5\text{I}_8$ level and their decay time are 0.35 and 0.25 ms, respectively, as depicted in Figure S5.

4 Conclusion

In summary, high-quality tetragonal phase $\text{Ba}_3\text{Sc}_2\text{F}_{12}$ nanosheets with uniform morphology and good dispersibility have been obtained via the thermal decomposition method. Then, we adjusted the doping contents of sensitizer Yb^{3+} and activator ions Er^{3+} or Ho^{3+} to get the strongest UC luminescent intensity, demonstrating that the optimum doping concentrations for $\text{Yb}^{3+}/\text{Er}^{3+}$ and $\text{Yb}^{3+}/\text{Ho}^{3+}$ are 25 mol%/4 mol% and 30 mol%/4 mol%,

respectively. Interestingly, when the Yb^{3+} doping concentration is more than 60 mol%, final products could transform from pure tetragonal phase $\text{Ba}_3\text{Sc}_2\text{F}_{12}$ to hexagonal $\text{Ba}_4\text{Yb}_3\text{F}_{17}$ nanocrystals. This study would provide a new kind of UC nanomaterials with strong red emission, and further complements the investigation of Sc-based nanomaterials, which may have promising applications that the Ln/Y-based materials don't possess.

Acknowledgements This study was financially supported by the National Natural Science Foundation of China (Nos. 11904323, 11874328 and 211902148) and the Certificate of Postdoctoral Research Grant in Henan Province (No. 1902014).

References

- [1] Gargas DJ, Chan EM, Ostrowski AD, Aloni S, Altoe MV, Barnard ES, Sanii B, Urban JJ, Milliron DJ, Cohen BE, Schuck PJ. Engineering bright sub-10-nm upconverting nanocrystals for single-molecule imaging. *Nat Nanotechnol.* 2014;9(4):300.
- [2] Czerny J, Heil F, Egbers CJ, Haase M. Size-controlled growth of $\beta\text{-NaGdF}_4$ and $\beta\text{-NaGdF}_4:\text{Yb, Er}$ nanocrystals: the influence of the surface area of NaF on the nucleation of the β -phase. *Chem Mater.* 2020;32(13):5691.
- [3] Wu Y, Xu J, Poh ET, Liang L, Liu H, Yang JKW, Qiu CW, Vallee RAL, Liu X. Upconversion superburst with sub-2 ms lifetime. *Nat Nanotechnol.* 2019;14(12):1110.
- [4] Ju Q, Tu D, Liu Y, Li R, Zhu H, Chen J, Chen Z, Huang M, Chen X. Amine-functionalized lanthanide-doped KGdF_4 nanocrystals as potential optical/magnetic multimodal bio-probes. *J Am Chem Soc.* 2012;134(2):1323.
- [5] Zhao JB, Wu LL. Yb^{3+} - and Er^{3+} -doped Y_2O_3 microcrystals for upconversion photoluminescence and energy transfer with enhancements of near-ultraviolet emission. *Rare Met.* 2019. <https://doi.org/10.1007/s12598-019-01269-4>.
- [6] Zuo SL, Chen P, Pan CF. Mechanism of magnetic field-modulated luminescence from lanthanide ions in inorganic crystal: a review. *Rare Met.* 2020. <https://doi.org/10.1007/s12598-020-01450-0>.
- [7] Xie J, Gao Z, Zhou E, Cheng X, Wang Y, Xie X, Huang L, Huang W. Insights into the growth mechanism of REF_3 (RE = La–Lu, Y) nanocrystals: hexagonal and/or orthorhombic. *Nanoscale.* 2017;9(41):15974.
- [8] Liu Y, Tu D, Zhu H, Chen X. Lanthanide-doped luminescent nanoprobes: controlled synthesis, optical spectroscopy, and bioapplications. *Chem Soc Rev.* 2013;42(1):6924.
- [9] Lin LS, Yang X, Zhou Z, Yang Z, Jacobson O, Liu Y, Yang A, Niu G, Song J, Yang HH, Chen X. Yolk–shell nanostructure: an ideal architecture to achieve harmonious integration of magnetic-plasmonic hybrid theranostic platform. *Adv Mater.* 2017; 29(21):1606681.
- [10] Lu F, Yang L, Ding Y, Zhu JJ. Highly emissive Nd^{3+} -sensitized multilayered upconversion nanoparticles for efficient 795 nm operated photodynamic therapy. *Adv Funct Mater.* 2016;26(26): 4778.
- [11] Wang Y, Zhou J, Gao J, Zhang K, Gao C, Xie X, Huang L. Physical manipulation of lanthanide-activated photoluminescence. *Ann Phys.* 2019;531(9):1900026.
- [12] Yang D, Ma P, Hou Z, Cheng Z, Li C, Lin J. Current advances in lanthanide ion (Ln^{3+})-based upconversion nanomaterials for drug delivery. *Chem Soc Rev.* 2015;44(6):1416.

- [13] Zhang K, Song S, Huang S, Yang L, Min Q, Wu X, Lu F, Zhu JJ. Lighting up MicroRNA in living cells by the disassembly of lock-like DNA-programmed UCNPs-AuNPs through the target cycling amplification strategy. *Small*. 2018;14:1802292.
- [14] Xue W, Di Z, Zhao Y, Zhang A, Li L. DNA-mediated coordinative assembly of upconversion hetero-nanostructures for targeted dual-modality imaging of cancer cells. *Chin Chem Lett*. 2019;30(4):899.
- [15] Yu S, Tu D, Lian W, Xu J, Chen X. Lanthanide-doped near-infrared II luminescent nanoprobe for bioapplications. *Sci China Mater*. 2019;62(8):1071.
- [16] Park YI, Lee KT, Suh YD, Hyeon T. Upconverting nanoparticles: a versatile platform for wide-field two-photon microscopy and multi-modal in vivo imaging. *Chem Soc Rev*. 2015;44(6):1302.
- [17] Ren N, Liang N, Yu X, Wang A, Xie J, Sun C. Ligand-free upconversion nanoparticles for cell labeling and their effects on stem cell differentiation. *Nanotechnology*. 2020;31(14):145101.
- [18] Liang L, Chen N, Jia Y, Ma Q, Wang J, Yuan Q, Tan W. Recent progress in engineering near-infrared persistent luminescence nanoprobe for time-resolved biosensing/bioimaging. *Nano Res*. 2019;12(6):1279.
- [19] Auzel F. Upconversion and anti-stokes processes with f and d ions in solids. *Chem Rev*. 2004;104(1):139.
- [20] Xie X, Li Z, Zhang Y, Guo S, Pendharkar AI, Lu M, Huang L, Huang W, Han G. Emerging approximately 800 nm excited lanthanide-doped upconversion nanoparticles. *Small*. 2017;13(6):1602843.
- [21] Zhou B, Shi B, Jin D, Liu X. Controlling upconversion nanocrystals for emerging applications. *Nat Nanotechnol*. 2015;10(11):924.
- [22] Zhou J, Liu Q, Feng W, Sun Y, Li F. Upconversion luminescent materials: advances and applications. *Chem Rev*. 2015;115(1):395.
- [23] Dong H, Du SR, Zheng XY, Lyu GM, Sun LD, Li LD, Zhang PZ, Zhang C, Yan CH. Lanthanide nanoparticles: from design toward bioimaging and therapy. *Chem Rev*. 2015;115(19):10725.
- [24] Zou W, Visser C, Maduro JA, Pshenichnikov MS, Hummelen JC. Broadband dye-sensitized upconversion of near-infrared light. *Nat Photon*. 2012;6(8):560.
- [25] Shen J, Chen G, Vu AM, Fan W, Bilsel OS, Chang CC, Han G. Engineering the upconversion nanoparticle excitation wavelength: cascade sensitization of tri-doped upconversion colloidal nanoparticles at 800 nm. *Adv Opt Mater*. 2013;1(9):644.
- [26] Feng W, Sun LD, Yan CH. Ag nanowires enhanced upconversion emission of NaYF₄: Yb, Er nanocrystals via a direct assembly method. *Chem Commun*. 2009;29(29):4393.
- [27] Wang F, Deng R, Wang J, Wang Q, Han Y, Zhu H, Chen X, Liu X. Tuning upconversion through energy migration in core-shell nanoparticles. *Nat Mater*. 2011;10(12):968.
- [28] Dou Q, Zhang Y. Tuning of the structure and emission spectra of upconversion nanocrystals by alkali ion doping. *Langmuir*. 2011;27(21):13236.
- [29] Wang F, Wang J, Liu X. Direct evidence of a surface quenching effect on size-dependent luminescence of upconversion nanoparticles. *Angew Chem Int Ed*. 2010;49(41):7456.
- [30] Wang J, Wang F, Wang C, Liu Z, Liu X. Single-band upconversion emission in lanthanide-doped KMnF₃ nanocrystals. *Angew Chem Int Ed*. 2011;50(44):10369.
- [31] Su Q, Han S, Xie X, Zhu H, Chen H, Chen CK, Liu RS, Chen X, Wang F, Liu X. The effect of surface coating on energy migration-mediated upconversion. *J Am Chem Soc*. 2012;134(51):20849.
- [32] Yuan P, Lee YH, Gnanasammandhan MK, Guan Z, Zhang Y, Xu QH. Plasmon enhanced upconversion luminescence of NaYF₄: Yb, Er@SiO₂@Ag core-shell nanocomposites for cell imaging. *Nanoscale*. 2012;4(16):5132.
- [33] Dong H, Sun LD, Wang YF, Ke J, Si R, Xiao JW, Lyu GW, Shi S, Yan CH. Efficient tailoring of upconversion selectivity by engineering local structure of lanthanides in Na_xREF_{3+x} nanocrystals. *J Am Chem Soc*. 2015;137(20):6569.
- [34] Li X, Zhang F, Zhao D. Lab on upconversion nanoparticles: optical properties and applications engineering via designed nanostructure. *Chem Soc Rev*. 2015;44(6):1346.
- [35] Ai Y, Tu D, Zheng W, Liu Y, Kong J, Hu P, Chen Z, Huang M, Chen X. Lanthanide-doped NaScF₄ nanoprobe: crystal structure, optical spectroscopy and biodetection. *Nanoscale*. 2013;5(14):6430.
- [36] Hu L, Chen J, Sanson A, Wu H, Rodriguez CG, Olivi L, Ren Y, Fan L, Deng J, Xing X. New Insights into the negative thermal expansion: direct experimental evidence for the “guitar-string” effect in cubic ScF₃. *J Am Chem Soc*. 2016;138(27):8320.
- [37] Hu L, Qin F, Sanson A, Huang LF, Pan Z, Li Q, Sun Q, Wang L, Guo F, Aydemir U, Ren Y, Sun C, Deng J, Aquilanti G, Rondinelli JM, Chen J, Xing X. Localized symmetry breaking for tuning thermal expansion in ScF₃ nanoscale frameworks. *J Am Chem Soc*. 2018;140(13):4477.
- [38] Xie J, Xie X, Mi C, Gao Z, Pan Y, Fan Q, Su H, Jin D, Huang L, Huang W. Controlled synthesis, evolution mechanisms, and luminescent properties of ScF_x: Ln (x = 2.76, 3) nanocrystals. *Chem Mater*. 2017;29(22):9758.
- [39] Teng X, Zhu Y, Wei W, Wang S, Huang J, Naccache R, Hu W, Tok AI, Han Y, Zhang Q, Fan Q, Huang W, Capobianco JA, Huang L. Lanthanide-doped Na_xScF_{3+x} nanocrystals: crystal structure evolution and multicolor tuning. *J Am Chem Soc*. 2012;134(20):8340.
- [40] Ding Y, Teng X, Zhu H, Wang L, Pei W, Zhu JJ, Huang L, Huang W. Orthorhombic KSc₂F₇: Yb/Er nanorods: controlled synthesis and strong red upconversion emission. *Nanoscale*. 2013;5(23):11928.
- [41] Fu H, Yang G, Gai S, Niu N, He F, Xu J, Yang P. Color-tunable and enhanced luminescence of well-defined sodium scandium fluoride nanocrystals. *Dalton Trans*. 2013;42(22):7863.
- [42] He X, Yan B. “One-stone-two-birds” modulation for Na₃ScF₆-based novel nanocrystals: simultaneous morphology evolution and luminescence tuning. *Cryst Growth Des*. 2014;14(7):3257.
- [43] Pei WB, Wang L, Wu J, Chen B, Wei W, Lau R, Huang L, Huang W. Controlled synthesis of uniform Na_xScF_{3+x} nanopolyhedrons, nanoplates, nanorods, and nanospheres using solvents. *Cryst Growth Des*. 2015;15(6):2988.
- [44] Wang Y, Yang B, Chen K, Zhou E, Zhang Q, Yin L, Xie X, Gu L, Huang L. Interconversion between KSc₂F₇: Er and K₂NaScF₆: Yb/Er nanocrystals: the role of chemistry. *Dalton Trans*. 2018;47(14):4950.
- [45] Zhao B, Shen D, Yang J, Hu S, Zhou X, Tang J. Lanthanide-doped Sr₂ScF₇ nanocrystals: controllable hydrothermal synthesis, the growth mechanism and tunable up/down conversion luminescence properties. *J Mater Chem C*. 2017;5(13):3264.
- [46] Wang W, Li YX, Hu SS, Zhang XM, Tang JF, Yang J. Hydrothermal synthesis of Ba₃Sc₂F₁₂: Yb³⁺, Ln³⁺ (Ln = Er, Ho, Tm) crystals and their up conversion white light emission. *RSC Adv*. 2017;7(89):56229.
- [47] Mai HX, Zhang YW, Si R, Yan ZG, Sun LD, You LP, Yan CH. High-quality sodium rare-earth fluoride nanocrystals: controlled synthesis and optical properties. *J Am Chem Soc*. 2006;128(19):6426.
- [48] Peng XG. Mechanisms for the shape-control and shape-evolution of colloidal semiconductor nanocrystals. *Adv Mater*. 2003;15(5):459.

- [49] Liu C, Wang H, Li X, Chen D. Monodisperse, size-tunable and highly efficient β - NaYF_4 : Yb, Er (Tm) up-conversion luminescent nanospheres: controllable synthesis and their surface modifications. *J Mater Chem*. 2009;19(21):3546.
- [50] Zheng G, Mourdikoudis S, Zhang Z. Plasmonic metallic heteromeric nanostructures. *Small*. 2020. <https://doi.org/10.1002/sml.202002588>.
- [51] Raj AN, Rinkel T, Haase M. Ostwald ripening, particle size focusing, and decomposition of sub-10 nm NaREF_4 (RE = La, Ce, Pr, Nd) nanocrystals. *Chem Mater*. 2014;26(19):5689.
- [52] Rinkel T, Nordmann J, Raj AN, Haase M. Ostwald-ripening and particle size focusing of sub-10 nm NaYF_4 upconversion nanocrystals. *Nanoscale*. 2014;6(23):14523.
- [53] Wei W, Zhang Y, Chen R, Goggi J, Ren N, Huang L, Bhakoo KK, Sun H, Tan TT. Cross relaxation induced pure red upconversion in activator- and sensitizer-rich lanthanide nanoparticles. *Chem Mater*. 2014;26(18):5183.
- [54] Chen G, Qiu H, Fan R, Hao S, Tan S, Yang C, Han G. Lanthanide-doped ultrasmall yttrium fluoride nanoparticles with enhanced multicolor upconversion photoluminescence. *J Mater Chem*. 2012;22(38):20190.